Materials Advances

ROYAL SOCIETY OF CHEMISTRY

PAPER

View Article Online
View Journal | View Issue

Cite this: *Mater. Adv.*, 2025, 6, 4286

Fabrication of a polypyrrole-functionalized biogenic $Mg(OH)_2$@MgO immunosensor, synthesized using *Graptopetalum paraguayense* leaf extract, for selective and efficient impedimetric detection of cholecalciferol (Vit-D_3)†

Sarita Shaktawat, Surendra K. Yadav and Jay Singh *

Vitamin D has gained significant global attention for its potential to prevent chronic conditions such as cancer, Parkinson's, Alzheimer's, cardiovascular disease, and osteoporosis. However, there are still no convenient techniques for interpreting the concentration Vit-D_3 in humans for diagnosis and monitoring. In this study, a B–$Mg(OH)_2$/MgO/PPy nanocomposite was hydrothermally synthesized using fresh leaves of the traditional Chinese medicinal plant *Graptopetalum paraguayense*, and confirmed by optoelectronic techniques. It is possible that this sustainable, chip-based, cost-efficient and cost-sensitive impedance biosensor can be used to quantify vitamin D3 concentration in humans. In this process, a sustainable BSA/Ab Vit-D/B–$Mg(OH)_2$@MgO/PPy NCs/ITO biosensor was fabricated that has neutral linker properties for immobilization of the antibody of Vit-D. The electrochemical performance of the biosensor was studied by EIS with linearity in the ΔR_{ct} value over the wide range of 1–200 nM with a limit of detection (LoD) of (0.026 nM) and sensitivity of 1.40 Ω nM^{-1} cm^{-2}. This ultrasensitive biosensor has excellent stability, reusability, a fast response time, and precise selectivity. Further validation of fabricated biosensors of Vit-D_3 was undertaken in real serum and spiked serum samples for a diagnostic approach. Therefore, the proposed sustainable, cost-effective, and sensitive biosensor shows promise for point-of-care diagnosis of vitamin-D-related diseases.

Received 1st March 2025,
Accepted 17th May 2025

DOI: 10.1039/d5ma00189g

rsc.li/materials-advances

1. Introduction

Lipophilic vitamin D (Vit-D) is a significant dietary supplement for the physiological actions of the human body. Conventionally, vitamin D is classified into two forms: vitamin-D_3 (Vit D_3 also called cholecalciferol) and vitamin-D_2 (Vit D_2 also called ergocalciferol).[1,2] Several studies show that Vit-D_3 is more potent than Vit-D_2.[2] Under exposure to UV radiation (wavelength 290 to 315 nm) 7-dehydrocholesterol is converted into previtamin-D_3, producing the final byproduct of Vit-D_3 in the body.[3] Vit-D_3 plays a crucial role in bone health by enhancing the absorption of calcium, magnesium, and phosphate, which are essential for normal bone development and maintenance. Numerous clinical studies have demonstrated that Vit-D_3 deficiency can be linked to various health issues. In children, this deficiency can lead to rickets, while in adults, it increases the risk of osteoporosis, characterized by weakened bones, increased risk of falls, and fragility fractures. Furthermore, Vit-D_3 deficiency has been associated with several serious health conditions, including hypertension, Parkinson's disease, Alzheimer's disease, cardiovascular diseases, and certain types of cancer.[4] Epidemiological studies conducted worldwide suggest that approximately 1 billion people suffer from Vit-D_3 deficiency. The National Institutes of Health (NIH) have published a Vit-D Fact Sheet for healthcare professionals, which includes information from laboratory animal studies. These studies indicate that Vit-D may inhibit carcinogenesis (the development of cancer) and slow tumor progression. Furthermore, some studies have investigated the effects of Vit-D supplementation on specific cancers, including breast cancer, colorectal cancer, lung cancer, pancreatic cancer, and prostate cancer.[5,6] The acceptable amount of Vit-D_3 in healthy human blood is 50 nM (20 ng mL^{-1}), whereas 30 nM

Department of Chemistry, Institute of Sciences, Banaras Hindu University, Varanasi 221005, Utter Pradesh, India. E-mail: jaysingh.chem@bhu.ac.in, jaimnnit@gmail.com; Tel: +91-9871766453

† Electronic supplementary information (ESI) available: Characterization techniques, binding energy data of Mg, O, C, and N elements of B-$Mg(OH)_2$@MgO/PPy NCs, Interference study of different interference towards the Vit-D_3, tabulated the real blood serum and spiked serum sample study % recovery, determination of concentration and % RSD toward the standard Vit-D_3 and CV graph of fabricated BSA/Ab Vit-D/B-$Mg(OH)_2$@MgO/PPy NCs/ITO biosensor towards Vit-D_3. See DOI: https://doi.org/10.1039/d5ma00189g

(12 ng mL^{-1}) is the lowest, and 125 nM (50 ng mL^{-1}) is the highest, which might be associated with weakening of bones and other health issues.[5] Currently, there is a critical need for accurate and efficient diagnostic and monitoring techniques for Vit-D_3. Several methods are routinely employed for its quantification, including competitive protein-binding (CPB) assays, radioimmunoassays (RIA), chemiluminescence immunoassays (CLIA), liquid chromatography (LC) with UV detection, liquid chromatography–mass spectrometry (LC–MS) or tandem mass spectrometry (LC–MS/MS),[7] fluorescence,[8] chromatography,[9] and capillary electrophoresis,[10] but these techniques often present challenges. They can be laborious and time-consuming, requiring expert handling for sample preparation, which can hinder their rapid and widespread implementation.

Today's priority is to find methods for the determination of Vit-D_3 that are not only sustainable but are also sensitive and selective. For a variety of applications, electrochemical biosensors provide several benefits over conventional laboratory methods. Among the salient characteristics of an electrochemical biosensor for Vit-D_3 are the need to be sensitive, selective, portable, affordable, reusable, and require minimal sample volume.[11,12] EIS is an advanced ultrasensitive monitoring technique that has been associated with the detection of interfacial properties of modified electrodes for the fabrication of sensors/biosensors.[13]

Nanoparticles continue to garner significant interest due to their diverse applications and unique properties. In a recent study, Gachpazan *et al.* developed an electrochemical biosensor for 25-hydroxyvitamin-D_3 utilizing truncated aptamers (VDBA14-23, VDBA14-27, and VDBA14-35) immobilized on $CuCo_2O_4$/N-CNTs/GCE. Their findings demonstrated that the VDBA14-35/$CuCo_2O_4$/N-CNT/GCE aptasensor exhibited the highest sensitivity within a 25-hydroxyvitamin D_3 concentration range of 1×10^{-13} to 1×10^{-6} M.[14] Bindu *et al.* reported a novel electrochemical sensor for Vit-D_3 detection in real samples using NiNPs-ZIF-8-modified@GCE. Here, nickel nanoparticles incorporating a zeolitic imidazolate framework (ZIF-8) were fabricated on a glassy carbon electrode for a dynamic range of detection from 0.025 to 25 μM with an LoD of 0.002 μM.[15] Chauhan *et al.* described aspartic-acid-functionalized gadolinium oxide nanorods for the efficient electrochemical detection of Vit-D_3 and Kaur *et al.* also reported an Au–MoS_2 hybrid immune-sensing platform for the voltammetric detection of Vit-D. While Bora *et al.* fabricated a nitrogen-doped, carbon-nanotube-based electrochemical detector for Vit-D_3 with a limit of detection of 16 pM in the 0–10 nM concentration range. These reported biosensors are heavy-metal-containing, toxic, and complex modification-based biosensors, but Barman *et al.* reported a Vit-D antibody functionalized MXene-based electrochemical biosensor for the point-of-care detection of Vit-D deficiency. Here a laser-induced graphene (LIG) MXene factionalized, and Vit-D immobilized electrode was implemented with an LoD of 1 pg mL^{-1} in the dynamic range 0.1–500 ng mL^{-1} in electrochemical DPV detection.[16] Nevertheless, today we need a conventional, sustainable, biocompatible, and less hazardous method as well as a more precise way to diagnose Vit-D_3.[17]

Due to the remarkable properties of MgO NPs, *e.g.* rapid charge transfer kinetics, stability, and high surface to volume ratio, they have found valuable applications in diverse fields. Owing to these properties, MgO NPs have been utilized in photocatalysis, energy storage, and electrochemical sensor/biosensor technologies. Polypyrrole (PPy) exhibits high electrical conductivity, typically ranging from 10 to 100 S^2 cm^{-1},[18] and excellent biocompatibility, redox, and ion exchange properties.[19] Singh *et al.* report on PPy-based emerging and futuristic hybrid nanocomposites that might play a role in biosensors/sensors. The linkage chemistry between the material and the antibody is influenced by the branching of the amine group and the Π–Π conjugation of PPy.[20] Nagaraj *et al.* synthesized a hybrid nanocomposite comprising magnesium oxide entrapped within a PPy matrix. This novel material demonstrates high efficiency and selectivity in scavenging fluoride ions from drinking water.[21] A fresh leaf extract from the traditional Chinese medicinal plant *Graptopetalum paraguyense* is utilized for the controlled nucleation of magnesium oxide nanoparticles. Then incorporated PPy was directly used for the selective detection of Vit-D_3. Sustainable approaches for the synthesis of B–$Mg(OH)_2$/MgO/PPy NCs and the direct immobilization of the antibody of Vit-D are possible due to the participation of PPy linkage chemistry.

2. Experimental section

2.1 Materials and methods

The materials used were absolute ethanol (Merck), $Mg(NO_3)_2 \cdot 6H_2O$ (magnesium nitrate hexahydrate, Merck), NaOH (Merck), anti-vitamin D receptor, clone 9A7 monoclonal antibody (Merck), Vit-D_3 (cholecalciferol, Merck), bovine serum albumin (BSA, Merck), sodium diphosphate anhydrous (Na_2HPO_4), sodium monophosphate (NaH_2PO_4) (Merck), potassium ferricyanide ($K_3[Fe(CN)_6]$), potassium ferrocyanide ($K_4[Fe(CN)_6]$), and an indium tin oxide (ITO) layer on glass for the substrate.

2.2 Preparation of *Graptopetalum paraguyense* plant extract

Fresh leaves of the traditional Chinese medicinal plant *Graptopetalum paraguyense* were collected and washed with DDQ water 2/3 times and dried. The leaves were cut into fine pieces and mashed with motorised pestles. Then 1 g of paste dissolved in 10 mL of DDQ water was heated at 65–70 °C for 30 min. This prepared solution was filtered through Whatman filter paper and the final extract was collected in a glass for further use in the reaction.

2.3 Synthesis of B–$Mg(OH)_2$@MgO/PPy NCs

Initially, 20 mL of 100 mM $Mg(NO_3)_2 \cdot H_2O$ in 20 mL of fresh *Graptopetalum paraguyense* leaf extract was continuously stirred for 30 min. Then 2 M NaOH was added slowly until the color changed from translucent to a brown precipitate and the pH rose to 12. This brownish precipitation was centrifuged at 10 000 rpm for 7 min 3 times with DDQ water and acetone and dried overnight at 70 °C. Moreover, 0.1 g of synthesized biogenic magnesium oxide nanoparticle (B–MgO) were

dissolved in 10 mL of DDQ water and ultrasonically treated for 1 h. Subsequently, 0.5 ml of pyrrole was gradually added to 1.35 g of $FeCl_3$ to initiate the oxidative polymerization of PPy, facilitating its incorporation onto the surface of B-MgO NPs. The reaction was allowed to proceed overnight to ensure complete polymerization and uniform surface integration. Then the synthesized sample was calcinated at 400 °C for 4 h and confirmed *via* optoelectronic characterization.

2.4 Formulation of calibration solution of Vit-D_3 and monoclonal antibody of Vit-D for electrochemical biosensing

For the electrochemical measurement of Vitamin D3, a formulated calibration solution with an initial concentration of 5 mM (19.23 mg in 10 mL of absolute ethanol) was diluted to a working concentration of 5 μM. Further dilutions were made in the calibration range of electrochemical sensors from 1 nM to 1000 nM of Vit-D_3. Excluding UV light, the open monoclonal antibody of Vit-D (25 μg) was dissolved in phosphate buffer (pH 7.4).

2.5 Fabrication of BSA/Ab Vit-D/B–$Mg(OH)_2$@MgO/PPy NCs/ITO immunoelectrode and mechanistic path for the electrochemical determination of Vit-D_3

Initially, B–$Mg(OH)_2$@MgO/PPy NCs were deposited on a functionalized ITO electrode using the electrophoretic deposition (EPD) method. The unique properties of PPy remove the need for linkers. Furthermore, the monoclonal antibody of Vit-D (Ab Vit-D), excluding UV light, was drip-coated on an B–$Mg(OH)_2$@MgO/PPy NCs/ITO electrode in a humid chamber overnight. The immobilized Ab Vit-D/B–$Mg(OH)_2$@MgO/PPy NCs/ITO electrode was washed with phosphate buffer (pH 7.0). The BSA/Ab Vit-D/B–$Mg(OH)_2$@MgO/PPy NCs/ITO electrode was then dried after applying BSA to prevent nonspecific adsorption. This ultimate immobilized BSA/Ab Vit-D/B–$Mg(OH)_2$@MgO/PPy NCs/ITO electrode was employed for frequency response analysis of Vit D_3. The process was conducted in the absence of UV light to prevent the sensitive reaction of Ab Vit-D with Vit-D_3. Fig. 1 shows a schematic illustration of the synthesis of B–$Mg(OH)_2$@MgO/PPy NCs, utilized in an impedance biosensor for Vit-D_3 to identify diseases caused by its relative excess or deficiency in the human body.

The mechanistic pathway for the electrochemical determination of Vit-D_3 in phosphate buffer containing 5 mM $[Fe(CN)_6]^{3-/4-}$ (0.9% NaCl, pH 5.7) using a three-electrode cell system. A fabricated working BSA/Ab Vit-D/B–$Mg(OH)_2$@MgO/PPy NCs/ITO electrode, dipped in $Fe^{2+/3+}$-containing phosphate buffer, showed redox antibody–antigen interaction with an increase in the concentration of Vit-D_3. Whereas the Ag/AgCl electrode retains the potential of the phosphate buffer, and the Pt electrode is resistant to oxidation.

2.6 Preparation of real serum and spiked serum samples

Further validation of the Vit-D_3 sensor was undertaken with real blood serum and real spiked serum samples. The centrifuged real blood serum sample for Vit-D was collected from the national reference lab, Pathkind Diagnostics Pvt. Ltd, Varanasi (India) for direct study. Whereas spiked serum samples were prepared in the laboratory by utilizing BSA (1 mg) in 7.0 pH phosphate buffer (1 mL) for further studies. The optoelectronic characterization techniques used to validate the synthesized B–$Mg(OH)_2$@MgO/PPy NCs are included in the ESI,† Section 2.7.

3. Results and discussion

3.1 XRD analysis

The X-ray diffraction (XRD) spectra (Fig. 2(a)) distinguished non-calcinated/calcinated B–$Mg(OH)_2$@MgO/PPy NCs. Whereas undifferentiated peaks in one spectrum (Fig. 2(a)-(i)) suggest an amorphous $Mg(OH)_2$ structure with the incorporation of amorphous PPy. Possible non-calcinated MgO/PPy NCs have broad peaks of amorphous conductive PPy at 10° ⟨2θ⟩ 20° and 30° ⟨2θ⟩ 50°,[22] and at 26.76°, 42.78°, and 80.49°, there are distinguishable peaks of the quartz glass surface where the sample was run on XRD.[23] While calcinated B–$Mg(OH)_2$@MgO/PPy NCs showed distinguishable sharp peaks of MgO/$Mg(OH)_2$ and little disappearance of PPy peaks in the spectra due to the gain in crystallinity of a bi-phasic nanocomposite with amalgamated PPy. The peaks at 2θ values of 33.1°, 35.4°, 49.6°, 57.9° and 71.7° correspond to the (100), (100), (101), (102), (110) and (103) lattice planes of $Mg(OH)_2$, respectively, whereas two peaks at 2θ values of 42.9° and 62.5° corresponding to the (200) and (220) lattice planes of MgO were confirmed by ICDD 00-044-1482 and 00-045-0946, respectively (Fig. 2(a)-(ii)).[24] The crystallite size of the B–$Mg(OH)_2$@MgO/PPy NCs was calculated with the Debye–Scherrer eqn (1), and the sharpest peak was found to be at a 2θ value of 35.4°, and the calculated average crystalline size was 1.38 nm.

$$D = \frac{k\lambda}{\beta \cos\theta} \quad (1)$$

where D is the crystallite size, k is the Scherrer constant (0.9), λ is the wavelength of the X-ray source of CuKα radiation (0.15406), β is the full width at half maximum (FWHM) of the more intense peak, and θ is the Bragg diffraction angle.

3.2 UV analysis

Fig. 2(b) displays the ultraviolet (UV) spectra of B–$Mg(OH)_2$@MgO/PPy NCs, illustrating absorbance as a function of wavelength within the 200–800 nm range, as no sharp peak can be observed. The energy band gap (E_g) was calculated using Tauc's relation:

$$(\alpha h\nu)^2 = A(h\nu - E_g)$$

were h is Planck's constant, A is a constant, α is the absorption coefficient, and E_g is the energy band gap. As B–$Mg(OH)_2$@MgO/PPy NCs is an insulator (E_g = 4.8 eV), defect states[25] and synergistic interaction with conductive PPy[26] were introduced to enhance electron delocalization and improve conductivity (Fig. 2(b) inset).

3.3 FTIR and Raman analysis

The intramolecular and intermolecular interaction of functional group bonds in B–$Mg(OH)_2$@MgO/PPy NCs was confirmed by the Fourier transform infrared (FTIR) spectra shown in Fig. 2(c).

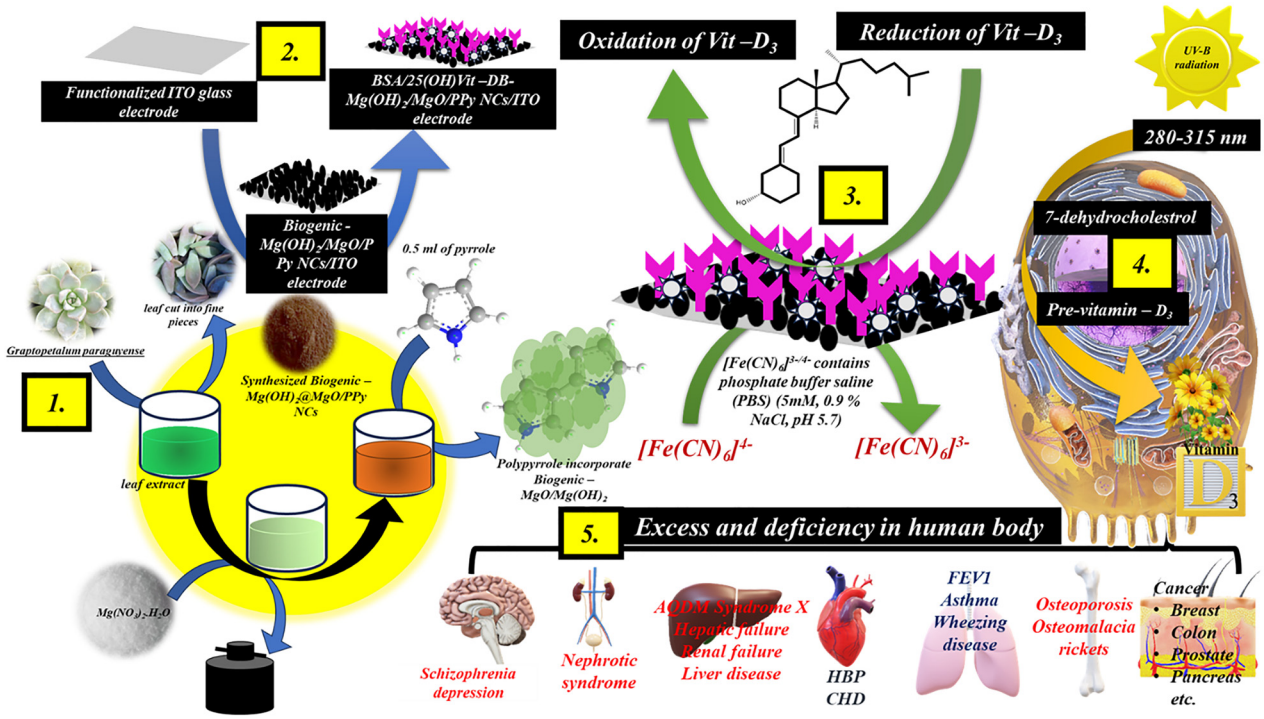

Fig. 1 Schematic illustration of the synthesis of B–Mg(OH)$_2$@MgO/PPy NCs by utilizing fresh leaves of the traditional medicinal plant *Graptopetalum paraguyense*, fabrication of impedance biosensor by modification on an ITO electrode, and the processes of Vit-D$_3$ in the human body in the presence of UV radiation (280–315 nm) as well as relative disease.

A broad peak at 3396 cm^{-1} of O–H bond stretching vibration is due to moisture absorption on the surface of the material.[11] Consequently, observed peaks at 2925 and 2858 cm^{-1} express C–H bond stretching and bending vibration[27] by interaction with the divalent Mg cation[28] of B–Mg(OH)$_2$@MgO. While at 1627 cm^{-1} the observed peak of the C=O bond could be the stretching vibration of the amide bond, extended π e$^-$ of NCs,[29] and 1384 and 1085 cm^{-1} are the C–N bond stretching

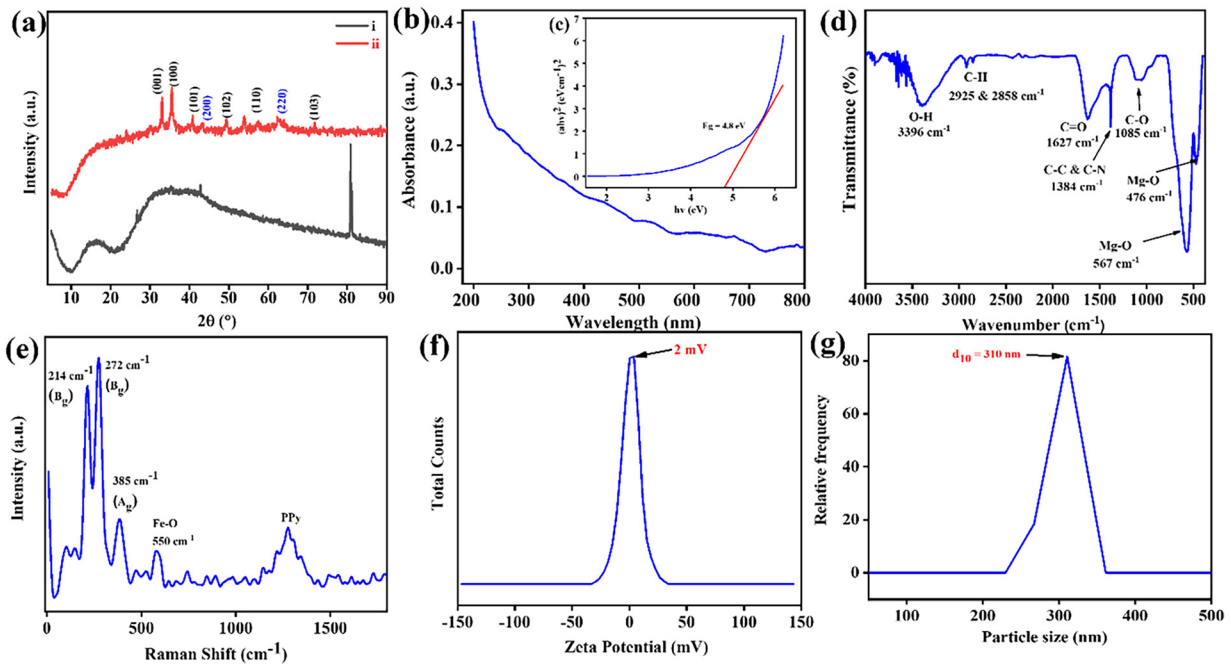

Fig. 2 Structural characterization of B–Mg(OH)$_2$@MgO/PPy NCs: (a) XRD spectra, (i) non-calcinated B–Mg(OH)$_2$@MgO/PPy NCs, (b) UV visible spectra and insert (c) Touc's plot of band gap, (d) FTIR spectra, (e) Raman spectra, (f) zeta potential spectra and (g) DLS spectra of B–Mg(OH)$_2$@MgO/PPy NCs, respectively.

vibration[30] of PPy. Whereas two continuous peaks at low-frequency regions 567 cm^{-1} and 476 cm^{-1} are the Mg–O bond stretching as well as bending vibration of $Mg(OH)_2$ and MgO bonds.

Raman spectroscopy, as depicted in Fig. 2(d), provides immediate support and validation for the proposed structural and compositional information regarding bond vibrations and stretching. Notably, lower-wavenumber scattered mode peaks are observed at 214 cm^{-1} (B_g), 272 cm^{-1} (B_g), 385 cm^{-1} (A_g), and 579 cm^{-1} (A_u), which can be attributed to B–$Mg(OH)_2$ and MgO bonds. Previous studies by Shaktawat *et al.* on biogenic magnesium oxide nanoparticles reported Raman and IR-active modes with distinct frequencies, irreducible representations, and point groups. Their reported spectra exhibited peaks at 670 cm^{-1} (B_u), 583 cm^{-1} (A_u), 385 cm^{-1} (A_g), 269 cm^{-1} (B_g), and 214 cm^{-1} (B_g), suggesting the presence of Mg–O bond scattered stretching vibrations within the MgO nanoparticles.[11] Conversely, a high-wavenumber broad peak observed at 1275 cm^{-1} is characteristic of the PPy moiety, specifically associated with the antisymmetric C–H in-plane bending and ring stretching vibrations.[31]

3.4 Zeta and DLS analysis

The size and dispersion ability of B–$Mg(OH)_2$@gO/PPy NCs are shown in Fig. 2(e). It has been observed that the low zeta potential of 2 mV would suggest that the B–$Mg(OH)_2$@MgO/PPy NCs are colloidally clustered, solid, and highly stable *via* Brownian motion.[32] Furthermore, from dynamic light scattering (DLS) analysis it was observed that the average particle size (d_{50}) is around 310 nm, suggesting possible agglomeration in PPy incorporated into B–$Mg(OH)_2$@MgO NCs, as shown in Fig. 2(f).[33]

3.5 XPS analysis

Successful direct immobilization of Ab Vit-D at the modified surface of the B–$Mg(OH)_2$@MgO/PPy NCs/ITO electrode was confirmed by the elemental binding energy of the surface using X-ray photoelectron spectroscopy (XPS) studies, as shown in Fig. 3. By using XPS-peak-41 software, each XPS spectrum was analyzed at high resolution by Shirley and linear background fitting with a deconvoluted peak. Fig. 3(a)(i)–(iii) show survey plots of B–$Mg(OH)_2$@MgO/PPy NCs/ITO, Ab Vit-D/B–$Mg(OH)_2$@MgO/PPy NCs/ITO and BSA/Ab Vit-D/B–$Mg(OH)_2$@MgO/PPy NCs/ITO, respectively (tabulated in Table 1). Survey plots ratify element binding energies, such as 55 eV Mg (2p), 100.35 Mg (2s), 283 eV C (1s), 397.9 eV N (1s), 494.6 eV for the core-level electron of O and 529.7 eV for O (1s). In Fig. 3(b)(i)–(iii), Shirley fitted asymmetric XPS spectra of Mg (2s) deconvoluted with peak intensities towards lower BE (ESI,† Table S1) would be influenced by a change in charge transfer after modification of the surface. A deconvoluted Mg (2s) has variable Mg^{2+} and Mg^{+} oxidation states, and its electronegativity is directly influenced by O as well as indirectly by C and N following the charge transfer. Analogously, in Fig. 3(c)-(i)–(iii) Shirley fitted asymmetric XPS spectra of O (1s) are deconvoluted. In Fig. 3(c)-(i)–(iii), deconvoluted peaks at 528 eV and 529 eV indicate lattice oxygen,[34] and 530.0 eV corresponds to vacancy oxygen,[35] representing chemisorbed oxygen (OH^{-}) species.[36] Fig. 3(c)-(ii), (iii) has the above-discussed deconvoluted peaks at 528.5 ± 0.1, 529.7 ± 0.3, and 530.3 ± 0.1 eV, respectively. Nevertheless, the additional peak at 533.7 eV is attributed to O═C–O.[37] Whereas the Shirley fitted asymmetric XPS spectrum of C 1s is deconvoluted in Fig. 3(d)-(i)–(iii). In Fig. 3(d)-(i) the deconvoluted peak

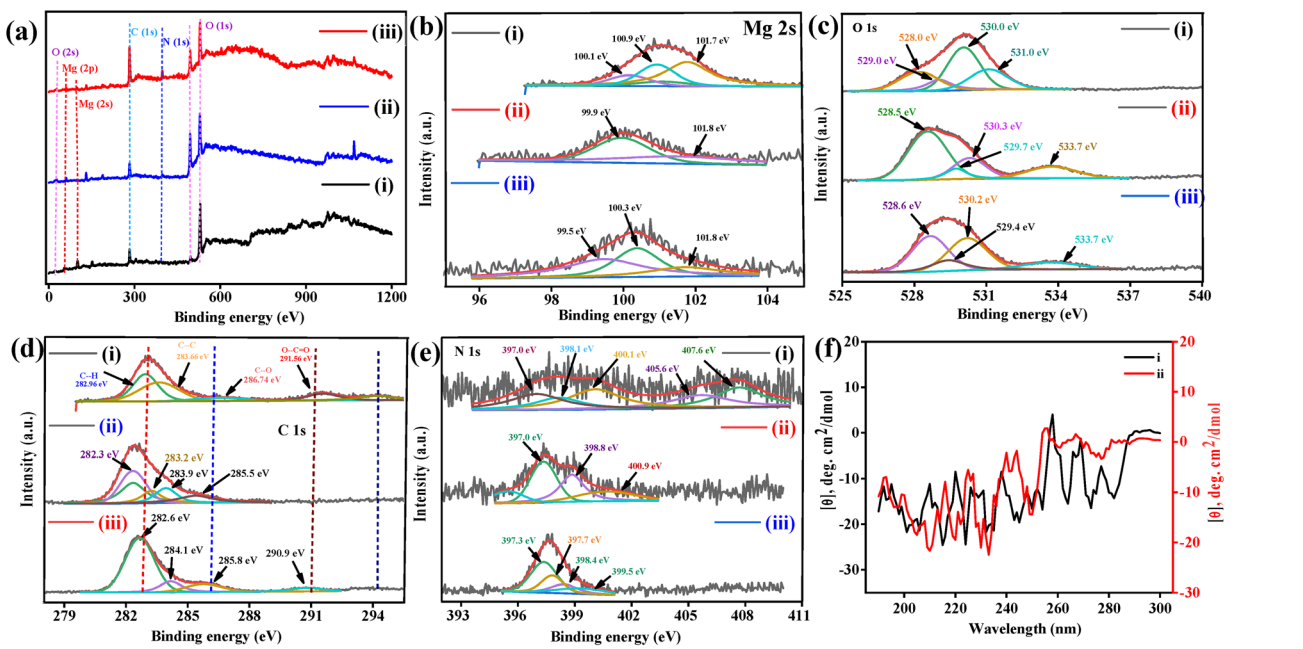

Fig. 3 XPS spectra of (i) B–$Mg(OH)_2$@MgO/PPy NCs relative binding energy and after immobilization of monoclonal antibody at that surface, (ii) Ab Vit-D/$Mg(OH)_2$@MgO/PPy NCs and (iii) final prepared impedance biosensor BSA/Ab Vit-D/$Mg(OH)_2$@MgO/PPy NCs, respectively. (a) Survey plot, (b) binding energy of Mg 2s, (c) binding energy of O 1s, (d) binding energy of C 1s, (e) binding energy of N 1s, respectively. (f) CD spectra of (i) B–$Mg(OH)_2$@MgO/PPy NCs and (ii) Ab Vit-D/B–$Mg(OH)_2$@MgO/PPy NCs, respectively.

Table 1 Summary of previously published research articles based on the electrochemical detection of Vit-D_3 along with their sensing performance

S. no.	Final electrode	Technique	Linearity	Sensitivity	LoD	Interference	Real sample	pH	Ref.
1.	VDBA14-35/$CuCo_2O_4$/N-CNT/GC	DPV	1×10^{-13} to 1×10^{-6} M	–	0.063 pM	25(OH)D_2, cholesterol, Na-deoxycholate	Aqueous solution and serum sample	1 mM $[Fe(CN)_6]^{3-/4-}$	14
2.	BSA/Ab-VD/Asp-Gd_2O_3 NRs/ITO	DPV	10–100 ng mL^{-1}	0.38 μA ng^{-1} mL^{-1} cm^{-2}	0.10 ng mL^{-1}	Ascorbic acid, cholesterol, glucose, oxalic acid, urea, and uric acid	–	7.0	4
3.	SPE graphite electrode modified with CYMAu@MNPs[a]	DPV	7.4–70 ng mL^{-1}		2.4 ng mL^{-1}	Glucose, glycine, ossalic acid, urea, and ascorbic acid	Serum sample	Phosphate buffer	50
4.	AbVD$_3$-ATP@AuNPs/RGO-SeO_2	EIS/CV	0.5–200 ng mL^{-1}	–	0.01 ng mL^{-1}	Glucose, ascorbic, cysteine, urea, oxalic acid, and cholesterol	Serum sample	7.4	51
5.	Aptamer-modified Au electrode	EIS	0.4–400 ng mL^{-1}		0.34 ng mL^{-1}		Serum sample	7.5(phosphate buffer)	52
6.	Au–Pd modified GCE	DPV	1–10 μM (Vit-D_2) and 5–50 μM (Vit-D_3)		0.15 and 0.18 μM	Vitamins A, K_1 and E		7.0	53
7.	BSA/Anti-VD/Fe_3O_4–PANnFs/ITO	DPV	0–100 ng mL^{-1}	0.90 μA ng^{-1} mL^{-1} cm^{-2}	0.12 ng mL^{-1}	Ascorbic acid, urea, uric acid, oxalic acid	–	6.0 (phosphate buffer)	54
8.	BSA/Ab Vit-D/B–Mg$(OH)_2$@MgO/PPy NCs/ITO electrode	EIS	1–200 ng mL^{-1}						This work

[a] CYM – cysteamine hydrochloride, MNP – magnetic nanoparticle.

of C 1s at 282.9 eV corresponds to C–H, 283.6 eV corresponds to conjugated C=C,[38] 286.7 eV is attributed to the PPy C–N species, and 291.5 eV may be lattice oxygen bonded to the carbon peak of O–C=O species.[39] In the case of Fig. 3(d)(ii), (iii), which has peaks at 282.3 ± 0.6 eV, 283.9 ± 0.6 eV (C–C) as discussed above, the peak shifted to lower BE at 285.5 ± 0.3 eV should be PPy C–N species. As in Fig. 3(d)(i), (iii) at 290.9 ± 1.5 eV, the satellite peak of C 1s would reflect the Π–Π interaction of the molecular structure.[31] In Fig. 3(e)-(i)–(iii) the Shirley fitted asymmetric XPS spectrum of the N 1s deconvoluted spectrum at 397.0 ± 0.3 eV shows the coexistence of C=N,[38] and 398.1 ± 0.8 eV corresponds to amine =N species,[31] 399.5 eV to C–N species,[38] and 400.1 ± 0.8 is a pyrrolic nitrogen configuration.[40] In addition to the 1s → σ* absorption band at 407 eV, there are 405.6 eV peaks belonging to the 1s →Π* feature.[41]

3.6 CD analysis

The circular dichroism (CD) spectra of B–Mg$(OH)_2$@MgO/PPy NCs and B–Mg$(OH)_2$/MgO/PPy NCs/Ab Vit-D are shown in Fig. 3(f)-(i) and (ii), respectively. The secondary structure of the random coil PPy incorporated into MgO, along with the direct interaction of the antibody at the composite surface, was analysed using BEST-SET software. The calculated structural configurations included a helix (58.6 and 58.7), antiparallel (35.2 and 32.3), parallel (6.1 and 9.1), and anti-3 (right twisted) (35.2 and 32.3), respectively. The results explore a possible random coil of B–Mg$(OH)_2$@MgO/PPy NCs interacting directly with the antibody of Vit-D.

3.7 TEM & HR-TEM analysis

Transmission electron microscopy (TEM) analysis was employed to evaluate the particle size distribution, *d*-spacing, and structural parameters of the B–Mg$(OH)_2$@MgO/PPy nanocomposites (NCs). Fig. 4(a)–(d) present TEM images at resolutions of 200 nm, 100 nm, 50 nm, and 10 nm, respectively, revealing uniformly distributed, round, froth-like particles of B–Mg$(OH)_2$@MgO/PPy NCs. Fig. 4(f) displays the selected area electron diffraction (SAED) pattern of B–Mg$(OH)_2$@MgO/PPy NCs. In the SAED image, corresponding bright ring planes (100) and (101) were calculated using ImageJ-win64 software, validated by ICDD 00-044-1482 and 00-045-0946 relative *d*-spacing values (2.48 and 1.92). The presence of distinct bright and dark fringes, resulting from diffraction of the electron beam, confirms the high degree of crystallinity within the B–Mg$(OH)_2$@MgO/PPy NCs. These TEM diffraction fringes and the SAED pattern collectively demonstrate the crystalline nature of the B–Mg$(OH)_2$@MgO/PPy NCs. The average particle size was determined to be 4.41 nm using image analysis software (ImageJ) and Lorentzian fitting.

3.8 SEM & EDX analysis

The micro/nano texture of the B–Mg$(OH)_2$@MgO/PPy NCs was characterized using scanning electron microscopy (SEM) analysis, as depicted in Fig. 4(g) and (h). The high-resolution SEM images at 2 μm and 1 μm (Fig. 4(g) and (h)) represent unequally

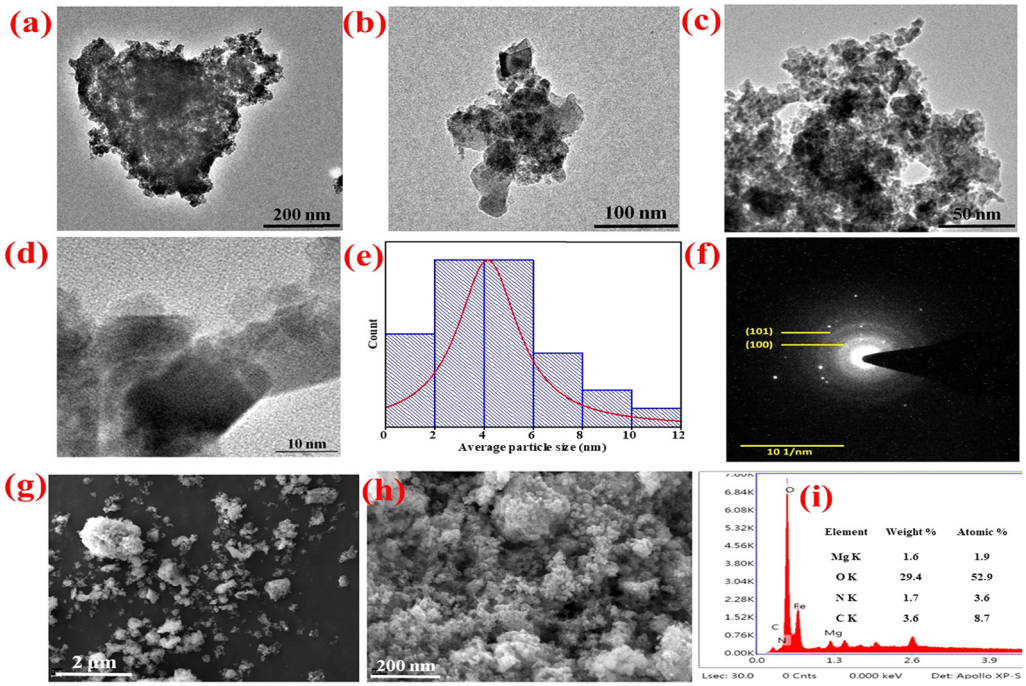

Fig. 4 TEM images of B–Mg(OH)@MgO/PPy NCs: (a) 200 nm, (b) 100 nm, (c) 50 nm and (d) 10 nm resolution, respectively, (e) histogram plot for average particle size, (f) SEAD pattern, (g) SEM image of B–Mg(OH)@MgO/PPy NCs of 2 μm resolution, (h) SEM image of B–Mg(OH)@MgO/PPy NCs of 200 nm resolution, and (i) EXD spectra in inserted table with element weight% and atomic%, respectively.

distributed particles, whereas Fig. 4(g) shows the froth-like texture of B–Mg(OH)$_2$@MgO/PPy NCs particles. SEM analysis of the electrode surface of the biosensor has been discussed in ESI,† Fig. S2. Energy-dispersive X-ray (EDX) spectra are shown in Fig. 4(i), while for elements Mg, O, N, and C weight% (1.6%, 29.4%, 1.7%, and 3.6%) and atomic% (1.9%, 52.9%, 3.6%, and 8.7%) are inserted in tables in the spectra.

4. Electrochemical analysis

The electrochemical performance of the BSA/Ab Vit-D/B–Mg(OH)$_2$@MgO/PPy NCs/ITO modified electrode was evaluated using cyclic voltammetry (CV) and electrochemical impedance spectroscopy (EIS). Both CV and EIS measurements were performed in phosphate-buffered saline (phosphate buffer) containing 5 mM $[Fe(CN)_6]^{3-/4-}$ (0.9% NaCl, pH 5.7). CV studies were conducted within a potential range of −0.3 V to 0.8 V at a constant scan rate of 50 mV s^{-1} throughout the experiments. Variations in the peak potential separation and peak current in CV measurements at the electrode surface are theoretically correlated to the electron transfer resistance and the electron transfer rate constant.[42]

EIS measurements were conducted under open-circuit potential conditions, with a frequency range spanning 0.01 Hz to 100 000 Hz and a signal amplitude of 10 mV. For all Vit-D$_3$ estimation experiments, the standardized set of parameters used for both CV and EIS studies was designated as the standard electrochemical setup (SES). EIS involves applying a small alternating current (AC) voltage to an electrochemical system and measuring the resulting current. Impedance, in this context, reflects the response of the system to this AC perturbation across a range of frequencies, providing insights into interfacial changes as a function of Vit-D$_3$ concentration. Conversely, CV analysis, which involves studying j_p variations within constant potential regions, proves valuable in optimizing various experimental parameters. These parameters include pH, scan rate, kinetic studies, reusability, response time, stability, interference studies, and analysis of real samples.

4.1 Electrochemical characterization of ITO surface modification by CV and EIS

Fabrication of the BSA/Ab Vit-D/B–Mg(OH)$_2$@MgO/PPy NCs/ITO electrode was successfully confirmed using CV and EIS measurements within the SES. Fig. 5(a) depicts the CV response of the bare ITO electrode, exhibiting two distinct redox peaks (I_{pa} = 0.52 mA cm^{-2}) corresponding to the reversible redox activity of the $[Fe(CN)_6]^{3-/4-}$ ions. The subsequent electrodeposition of B–Mg(OH)$_2$@MgO/PPy NCs onto the ITO surface *via* the EPD method significantly enhanced the anodic current (I_{pa} = 0.81 mA cm^{-2}) and accelerated the reaction rate at the electrode surface. This improvement in I_{pa} can be attributed to the increased electroactive surface area due to the improved surface-to-volume ratio of the composite material. Following the immobilization of Ab Vit-D, the anodic current (I_{pa}) of the B–Mg(OH)$_2$@MgO/PPy NCs/ITO biosensor decreased slightly to 0.78 mA cm^{-2}. This observation suggests that the immobilized Ab Vit-D partially hinders the electron transfer of $[Fe(CN)_6]^{3-/4-}$

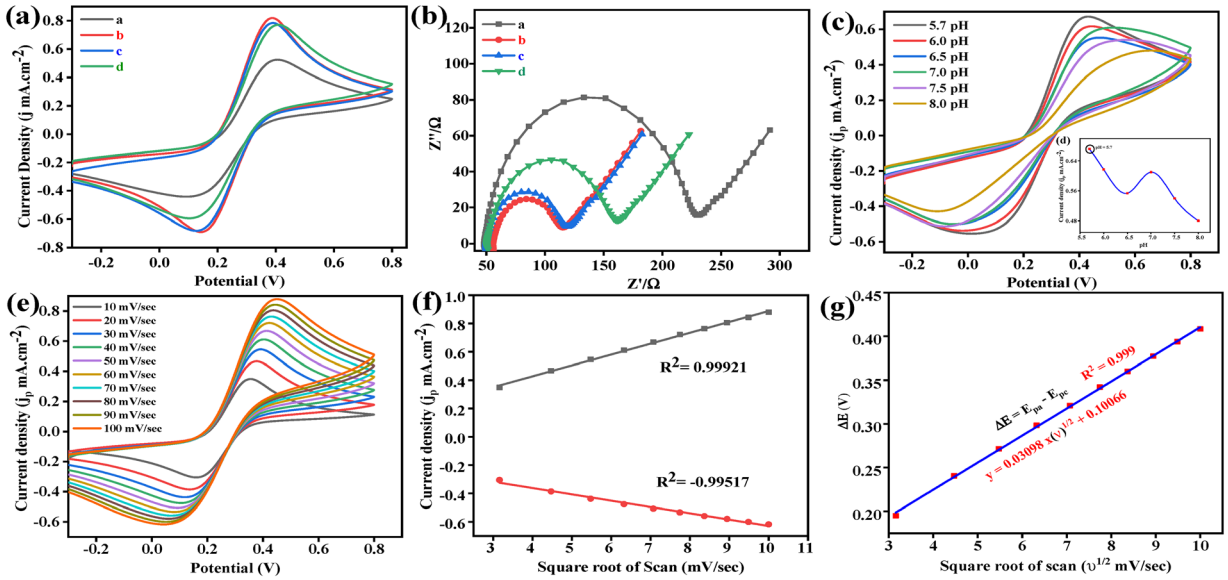

Fig. 5 Electrochemical studies of (a) B–Mg(OH)$_2$@MgO/PPy NCs/ITO electrode in [Fe(CN)6]$^{3-/4-}$-containing phosphate buffer (5 mM, 0.9% NaCl, pH 5.7): (a) CV spectra of fabricated impedance biosensor for Vit-D$_3$ for (a) bare ITO, (b) B–Mg(OH)$_2$@MgO/PPy NCs/ITO, (c) Ab Vit-D/B–Mg(OH)$_2$@MgO/PPy NCs/ITO and (d) BSA/Ab Vit-D/B–Mg(OH)$_2$@MgO/PPy NCs/ITO electrodes, respectively. (b) Further validation of this fabricated biosensor by EIS (Nyquist plot). (c) pH optimization at SES in inserted line + symbol graph, have maximum optimized pH 5.7. (e) Scan rate CV graph (10–100 mV s^{-1}) of B–Mg(OH)$_2$@MgO/PPy NCs. (f) Calibration fitting plot of redox peak maxima of j_p towards scan rate ($v^{1/2}$). (g) Calibration fitting plot of redox peak maxima potential (V) toward ($v^{1/2}$), respectively.

ions at the ITO interface. Finally, the introduction of BSA resulted in a minimal change in the anodic current (I_{pa} = 0.77 mA cm^{-2}), indicating that BSA effectively blocks nonspecific binding sites on Ab Vit-D without interfering with the electron transfer process at the ITO interface.

Furthermore, EIS measurements effectively assess the changes in the electrical properties of the ITO surface modifications. To scrutinize each modification step on the ITO electrode, EIS measurements were performed in 5 mM [Fe(CN)$_6$]$^{3-/4-}$-containing phosphate buffer (0.9% NaCl, pH 5.7) within a frequency range of 0.01 to 100 000 Hz at a signal amplitude of 10 mV. The Nyquist plot obtained from EIS analysis typically exhibits a semicircular portion at higher frequencies and a linear part at lower frequencies. The semicircular portion reflects electron transfer resistance, while the linear segment indicates controlled diffusion. Fig. 5(b) presents the Nyquist plots for bare ITO, B–Mg(OH)$_2$@MgO/PPy NCs/ITO, Ab Vit-D/B–Mg(OH)$_2$@MgO/PPy NCs/ITO, and BSA/Ab Vit-D/B–Mg(OH)$_2$@MgO/PPy NCs/ITO modified electrodes. The bare ITO electrode displays a large semicircle with a correspondingly high charge transfer resistance (R_{ct}). Upon modification with B–Mg(OH)$_2$@MgO/PPy NCs, the semicircle diameter decreases, signifying a reduction in R_{ct} and an enhancement in the electron transfer rate. Subsequently, the immobilization of Ab Vit-D leads to a slight increase in R_{ct}, indicating partial hindrance to electron transfer between the substrate solution and the ITO surface. The observed harmony between the CV curves and the Nyquist plots confirms the excellent electronic properties of the B–Mg(OH)$_2$@MgO/PPy NCs/ITO electrode. The electrochemical characterization collectively demonstrates the successful immobilization of each respective component on the electrode surface, providing a solid foundation for further investigation.

4.2 pH optimization

The optimum pH for maximizing the electrochemical behavior of the BSA/Ab Vit-D/B–Mg(OH)$_2$@MgO/PPy NCs/ITO electrode was determined within the pH range of 5.7 to 8.0 using phosphate buffer. CV measurements were performed with the [Fe(CN)$_6$]$^{3-/4-}$ redox couple under SES conditions, as shown in Fig. 5(c). The maximum j_p was observed at pH 5.7, suggesting optimal electron flow between the electrode ($Mg^{+/2+}$) and the redox couple ([Fe(CN)$_6$]$^{3-/4-}$), as depicted in Fig. 5(d). While pH 7.5 also provides a favorable environment for the electrochemical reactions of the BSA/Ab Vit-D/B–Mg(OH)$_2$@MgO/PPy NCs/ITO electrode.

4.3 Electrokinetic study of BSA/Ab Vit-D/B–Mg(OH)$_2$@MgO/PPy NCs/ITO electrode

Scan rate studies are used to observe the kinetics of the electrochemical reaction of the modified electrode. Increasing the scan rate consequently decreases the size of the diffusion layer, confirmed by a simultaneous increase in j_p.[43] Fig. 5(e) shows a variation in scan rate from 10 to 100 mV s^{-1} in the potential range of −0.3 V to 0.8 V, consequently simultaneously increasing oxidation (I_{pa}) and reduction (I_{pc}) peaks j_p with shifts in the potential towards more positive and negative directions, respectively (Fig. 5(f)). The observed peak potential separation ($\Delta E = E_{pa} - E_{pc}$) ranged between 0.2 and 0.4 mV with ΔE maintained within the range of 0.25 to 0.57 mV, indicating a quasi-reversible redox process. A strong linear relationship was observed between peak potential and the square root of the scan rate (R^2 = 0.999), described by the equation $y(V)$ = $0.03098x(\nu^{1/2})$ + 0.10066, as illustrated in Fig. 5(g). Fast

electrode kinetics were observed, as evidenced by the simultaneous increase in the peak potential separation (ΔE) with increasing scan rate. This observation confirms the quasi-reversible nature of the electrochemical process. Furthermore, the linear increase in the magnitude of both anodic (I_{pa}) and cathodic (I_{pc}) peak currents with the square root of the scan rate ($v^{1/2}$), as shown in Fig. 5(e), indicates that the process is diffusion-controlled. The overall reaction rate at the BSA/Ab Vit-D/B–Mg(OH)$_2$@MgO/PPy NCs/ITO electrode surface in an electrochemical cell is determined by the electrochemical reactions occurring at the electrode–electrolyte interface. In this case, the electrochemical reaction kinetics were evaluated by determining the charge transfer rate constant (K_s) using the Laviron equation:[44]

$$K_s = \frac{mnFv}{RT} \quad (2)$$

where the Faraday constant (F = 96 500C mol^{-1}), the peak-to-peak separation m (V), the number of transferred electrons (n = 1), the gas constant (R = 8.314 J K^{-1} mol^{-1}), the scan rate v (50 mV s^{-1}), and room temperature (T = 25 °C) are used. The calculated electron transfer rate constant (K_s) of 2.28 s^{-1} for the BSA/Ab Vit-D/B-Mg(OH)@MgO/PPy NCs/ITO electrode indicates enhanced electron transfer kinetics, attributed to the superior electrocatalytic activity of the B-Mg(OH)@MgO/PPy NCs. The electroactive surface area was determined by the Randles–Ševčík equation for quasi-reversible systems:

$$I_p = (2.69 \times 10^5)n^{3/2}AD^{1/2}Cv^{1/2} \quad (3)$$

where the anodic peak current, cathodic peak current, and peak current of the relative electrode are denoted by I_{pa}, I_{pc}, and I_p, respectively. The surface area of the electrode (A = 1 cm^2), the surface concentration (C = 5 mM), the number of electrons (n = 1), the diffusion coefficient D, and the scan rate (v = 50 mV s^{-1}) were used for the calculations. The value of D for the BSA/Ab Vit-D/B–Mg(OH)$_2$@MgO/PPy NCs/ITO electrode is 0.21 cm^2 s^{-1}. The surface concentration of the BSA/Ab Vit-D/B–Mg(OH)$_2$@MgO/PPy NCs/ITO electrode was calculated with the Brown–Anson model:

$$I_p = \frac{n^2F^2I^*AV}{4RT} \quad (4)$$

where the Faraday constant F, gas constant (R = 8.314 J K^{-1} mol^{-1}), electron number (n = 1), surface concentration I^* of the corresponding electrode, the surface area of the electrode (A = 0.25 cm^2), the scan rate (V = 50 mV^{-1}), and the temperature (T = 25 °C) were utilized to calculate the parameters. The observed surface concentration (I^*) of the BSA/Ab Vit-D/B–Mg(OH)$_2$@MgO/PPy NCs/ITO electrode was 3.26 mol cm^{-2}.

4.4 EIS response of Vit-D$_3$ towards the BSA/Ab Vit-D/B–Mg(OH)$_2$@MgO/PPy NCs/ITO electrode

Qualitative and quantitative evaluations are necessary for an accurate diagnosis of Vit-D$_3$. Investigations of the BSA/Ab Vit-D/B–Mg(OH)$_2$@MgO/PPy NCs/ITO biosensor were carried out using EIS.[45] Contemporarily, various research articles have been published on the diagnosis of Vit-D$_3$, but increasingly eco-friendly approaches are still required. MgO based composites with moderate sensitivity have been reported for the detection of various analytes, including glucose, mRNA, hemoglobin, and vitamin B$_{12}$. The corresponding sensing platforms include CH-Zn-MgO-Gox for glucose,[46] AuNPs/MgO/GCE,[47] Nafion/Hb/MgO@CNFs/CILE,[48] B–MgO NPs,[11] respectively. To detect Vit-D$_3$ using impedance, the fabricated biosensor

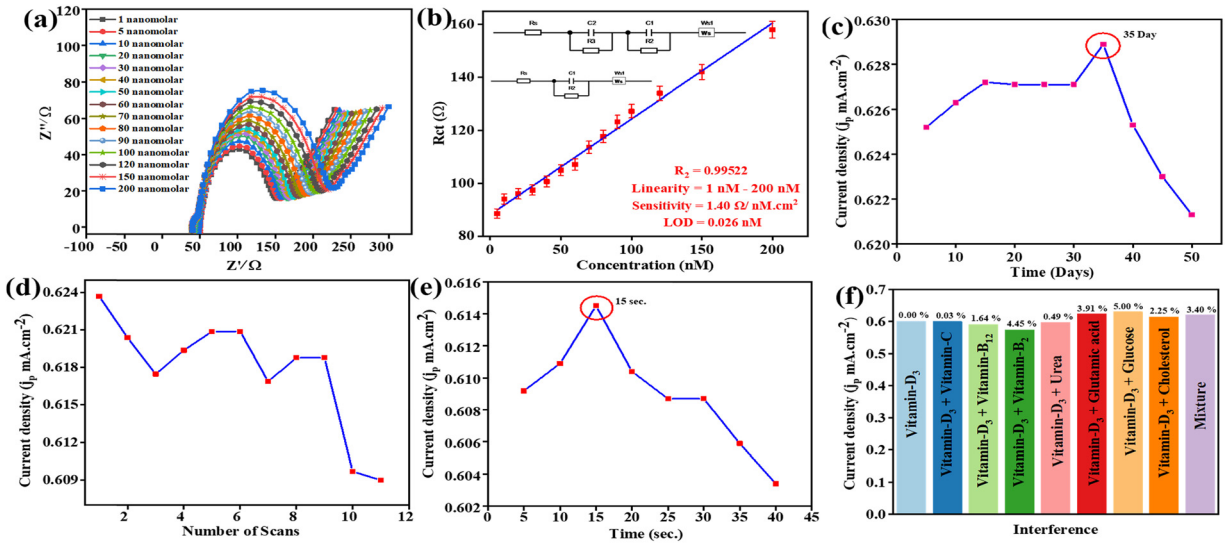

Fig. 6 Impedance biosensor of Vit-D$_3$ studies in $[Fe(CN)_6]^{3-/4-}$-containing phosphate buffer (5 mM, 0.9% NaCl, pH 5.7). (a) Nyquist plot of (Z' real/Ω) *vs.* ($-Z''$ imaginary/Ω) of BSA/Ab Vit-D/B–Mg(OH)$_2$@MgO/PPy NCs/ITO biosensor impedance sensing in the linear range of 1–200 nM concentration of Vit-D$_3$. (b) Calibration plot in the linear range of 1–200 nM concentration of Vit-D$_3$ with two possible fitted circuits inserted. (c)–(f) CV study line + symbol plots in constant SES as well as in the potential range −0.3 V to 0.8 V at a scan rate of 50 mV s^{-1} of stability, reusability, response time and interference studies, respectively.

examines the modified BSA/Ab Vit-D/B–$Mg(OH)_2$@MgO/PPy NCs/ITO electrode. The Nyquist plot of Z' (real) *vs.* $-Z''$ (imaginary) of the BSA/Ab Vit-D/B–$Mg(OH)_2$@MgO/PPy NCs/ITO biosensor by impedimetric analysis of Vit-D_3 is shown in Fig. 6(a), with a linear concentration range of 1–200 nM. Consequently, an increase in vitamin D concentration corresponds to an increase in the diameter of the semicircle in the Nyquist plot, indicating a higher charge transfer resistance (R_{ct}). Moreover, the Nyquist plot has a semicircle at some $Z' > 0$ (series resistance, R_s), where the width of the semicircle is R_{ct}, and a straight line with a 45° angle describes diffusion in the EIS process.[49] Two semicircles were seen with linearly increasing concentrations greater than 20 nM of Vit-D_3 on the BSA/Ab Vit-D/B–$Mg(OH)_2$@MgO/PPy NCs/ITO electrode. Two interfaces are present at the working electrode surface in the electrolyte: the higher antibody–antigen interface concentration (20–200 nM) (Equivalent circuit B), for the BSA/Ab Vit-D/B–$Mg(OH)_2$@MgO/PPy NCs/ITO electrode, and phosphate buffer interface concentration 1–20 nM (Equivalent circuit A). The lower concentration is not able to provide a strong signal due to the antibody–antigen interface; hence, it is not seen in the equivalent circuit. The contribution from that interface has been combined and is seen in one interface only. The observed sensitivity towards Vit-D_3 by the fabricated biosensor is 1.40 Ω nM^{-1} cm^{-2}, in the linear range of concentration 1–200 nM, with a limit of detection (LoD) of 0.026 nM, with the lowest linear error fit regression coefficient (R^2 = 0.99522). The results of the linear fit of the EIS synthesised information toward Vit-D_3 are shown in Fig. 6(b) with their respective equivalent circuits. Here R_s is the resistance of circuit components, wires, and instrumental hindrance, C_1 and C_2 are the double-layer capacitances designated for the different interfaces, R_2 and R_3 are the resistors, and W_s is the Warburg short, manifesting a 45° line on the low-frequency side. The mentioned equivalent circuits synthesise the information that responds linearly as a function of Vit-D_3.

Table 1 presents a comparative study of previously reported research articles for the detection of Vit-D_3 along with their sensing performance. In these reports, heavy metal and metal oxide based electrochemical biosensors have been used for CV and DPV techniques, but these techniques are not much more informative and using heavy metals is hazarous. This work presents an environmentally friendly approach to fabricate an impedance biosensor for Vitamin D_3 to address aforementioned challenge.

4.5 Competence of the fabricated BSA/Ab Vit-D/B–$Mg(OH)_2$@MgO/PPy NCs/ITO biosensor for Vit-D_3

The BSA/Ab Vit-D/B–$Mg(OH)_2$@MgO/PPy NCs/ITO electrode for Vit-D_3 at 70 nM 10 μL^{-1} was optimized by CV studies at SES. The stability of the fabricated biosensor towards Vit-D_3 was confirmed by storage of electrode for 50–55-days at a temperature of 4 °C. There was a rise in j_p until day 35, when the maximum was reached, after that a continuous decrease in stability was confirmed by a decrease in j_p (Fig. 6(c)). These CV study results confirm that the fabricated BSA/Ab Vit-D/B–$Mg(OH)_2$@MgO/PPy NCs/ITO biosensor shows excellent efficacy towards Vit-D_3. The repeatability of the fabricated biosensor was estimated by 11 successive scans of CV with Vit-D_3 (70 nM 10 μL^{-1}). The fabricated impedance biosensor displays substantial repeatability with a% RSD of ±1.8% toward Vit-D_3, and after 9 scans the optimized decrease in j_p is shown in Fig. 6(d). The fabricated biosensor exhibits a maximum peak response (j_p = 0.61 mA cm^{-2}) at 15 s (% RSD = 1.4%) during 40 s/5 s CV testing (Fig. 6(e)). The results confirm that the fabricated BSA/Ab Vit-D/B–$Mg(OH)_2$@MgO/PPy NCs/ITO biosensor showed good stability, excellent reusability, and better response time towards the impedimetric detection of Vit-D_3. Repeatability and reproducibility studies are discussed in the ESI† with Fig. S3 and S4.

4.6 Interference and selectivity study

The selectivity of the impedance BSA/Ab Vit-D/B–$Mg(OH)_2$@MgO/PPy NCs/ITO biosensor for Vit-D_3 was examined by an interference CV study with different analytes, as shown in Fig. 6(c). Here, CV is employed to assess the efficacy of the biosensor, as it provides critical insights into its capacity to detect psychological interferences. The selectivity of the biosensor was evaluated by investigating the influence of potential interferents, including vitamin B_2, vitamin B_{12}, vitamin C, urea, glutamic acid, glucose, and cholesterol. These interferents were introduced into phosphate buffer (pH 5.6, containing 0.9% NaCl and 5 mM $[Fe(CN)_6]^{3-/4-}$ as the redox couple) at a scan rate of 50 mV s^{-1} within a potential range of −0.3 V to 0.8 V. The results are summarized in ESI† Table S2 and visualized graphically in Fig. 6(c) as a bar graph. This figure illustrates the effect of these interferents on the anodic peak current (I_{pa}) of 70 nM standard Vit-D_3 in buffer. I_{pa} exhibited a minimal reduction of less than ±5.0% RSD in the presence of these interferents. These findings indicate that the interfering substances had a negligible effect on the electrochemical current response to variations in Vit-D_3 concentration, thereby demonstrating the high selectivity of the biosensor for monitoring Vit-D_3 in real samples.

4.7 Real sample analysis

The performance of the biosensor was evaluated using human serum samples of individuals deficient in Vit-D_3 to provide more favourable data in real-world applications, and bovine serum albumin (BSA spiked serum sample) was used for further validation, as shown in Fig. 7. For this, blood serum (BS) from individuals with insufficient Vit-D_3 and spiked serum were prepared in different standard Vit-D_3. A blood serum and spiked BSA sample was added to different concentrations of standard Vit-D_3 for the electrochemical detection of Vit-D_3. The deviation of linear standard Vit-D_3 variable concentrations with blood serum and spiked serum samples is tabulated in ESI,† Table S3.

The concentration of Vit-D_3 in this sample was identified by comparing the j_p value obtained from unknown serum and spiked samples with the standard Vit-D_3 concentrations of 1 nM, 5 nM, 30 nM, 60 nM, 90 nM, 120 nM, 150 nM, and

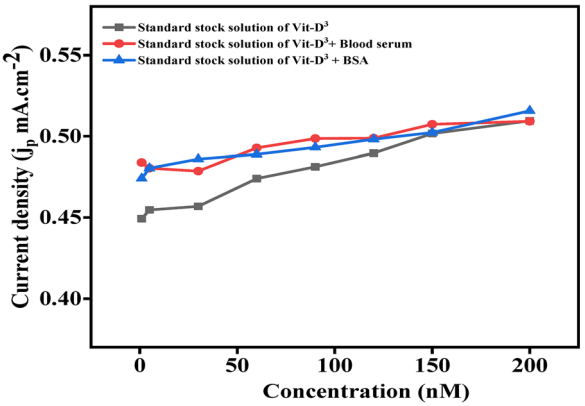

Fig. 7 Line + symbol plot of real-sample studies of Vit-D_3 by CV in $[Fe(CN)_6]^{3-/4-}$-containing phosphate buffer (5 mM, 0.9% NaCl, pH 5.7) in −0.3 to 0.8 V at 50 mV s^{-1} of the fabricated impedance biosensor in real serum samples and spiked serum samples with respect to standard Vit-D_3 concentration.

200 nM, where the obtained concentrations were 1.07 nM, 5.28 nM, 31.42 nM, 62.37 nM, 93.23 nM, 122.25 nM, 151.70 nM and 200 nM for blood serum samples, and 1.05 nM, 5.28 nM, 31.91 nM, 61.88 nM, 92.22 nM, 122.10 nM, 150.17 nM and 202.43 nM for spiked samples. Standard Vit-D_3 showed deviation from concentration by ±2/3 nM with maximum% recoveries of 107.7% and 106.3%, an % RSD of 7.7% and 6.3% for blood serum and spiked serum samples, respectively.

4.8 Laboratory testing validates the biosensor

To determine the amount of Vit-D_3 in the same serum sample, a Vit-D_3 assay was conducted in the laboratory of the national reference laboratory, Pathkind Diagnostics Pvt. Ltd, Varanasi (India). To test the sensitivity of the developed biosensor, the same serum samples were also assessed for Vit-D 25-hydroxy using the ELISA technique (the relative detection report is given in ESI†). It was found that the ELISA kit claimed to work below 60 nM, while the clinical cutoff value for total Vit-D is 25–60 nM. Fabricated electrochemical biosensors have a linear range of detection of 1–200 nM with an LoD of 0.026 nM; the results show a conventional diagnostic approach for Vit-D_3.

5. Conclusions

The fabrication of a sustainable electrochemical biosensor BSA/Ab Vit-D/B–$Mg(OH)_2$@MgO/PPy NCs/ITO for the diagnosis of Vit-D_3 *via* B–$Mg(OH)_2$@MgO/PPy NCs synthesized using the hydrothermal method. Initially, B–$Mg(OH)_2$@MgO/PPy NCs synthesized by utilizing fresh leaf extract of the traditional Chinese medicinal plant *Graptopetalum paraguyense*. These sustainable B–$Mg(OH)_2$@MgO/PPy NCs were modified ITO by the EPD method and utilized for the electrochemical diagnosis of Vit-D_3, after immobilization of a monoclonal antibody of Vit-D by the humate process. The synthesized material and fabricated electrodes were characterized by different optoelectronic techniques. This fabricated biosensor was realized by using CV and DPV techniques and was validated by improved electrochemical activity, enhanced electro-oxidation behaviour, and outstanding selectivity and sensitivity for extremely minimal Vit-D_3 concentrations. Kinetic study of the fabricated BSA/Ab Vit-D/B–$Mg(OH)_2$@MgO/PPy NCs/ITO electrode shows high catalytic behaviour (K_s = 2.28 s^{-1}), diffusion control (D = 0.21 cm^2 s^{-1}), and observed surface concentration (I^* = 3.26 mol cm^{-2}). The calculated sensitivity of the electrode was 1.40 Ω nM^{-1} cm^{-2}, regression coefficient (R^2 = 0.99522) with an LoD of 0.026 nM in the linear range of concentration from 1 to 200 nM by EIS studies. The observed sensitivity reflects the fact that the fabricated biosensor shows sensitive and selective detection for Vit-D_3. The substantial results of fabricated biosensors have been utilized for point-of-care detection due to the rapid response time (15 s with % RSD of ±1.8%), reusability (9 scans with % RSD of ±1.4%), and stability (35 days), for the accurate detection of Vit-D_3. This environmentally friendly value enables integrated diagnostic devices to be used for the real-time monitoring of Vit-D_3 levels for individuals to regulate relative deficiency/efficiency. The synthesized material was utilized in different biosensing applications for the detection of various analytes for human health monitoring.

Author's contribution

S. S.: data curation, investigation, visualization, writing – original draft. S. K. Y.: data curation, EIS experiment setup, equivalent circuit modeling, EIS data fitting, data validation, writing – review & editing of the original draft, and J. S.: conceptualization, validation, project administration, resources, supervision, writing – review & editing of the original draft.

Data availability

The data supporting this article have been included as part of the ESI.†

Conflicts of interest

The authors declare that they have no known competing financial interests or personal relationships that could have appeared to influence the work reported in this paper.

Acknowledgements

This work received no specific grant from public, commercial, or not-for-profit funding agencies. S. S. is thankful to his affiliated institution for providing constant financial support. S. K. Y. is thankful to BHU for (IoE MPDF Award number 55770, and J. S. acknowledges BHU for) providing a seed grant and BRIDGE grant under the MoE Govt. India, Institute of Eminence (IoE), under Dev. Scheme no. 6031 & 6031A respectively.

References

1 L. A. G. Armas, B. W. Hollis and R. P. Heaney, *J. Clin. Endocrinol. Metab.*, 2004, **89**, 5387–5391.

2 R. P. Heaney, R. R. Recker, J. Grote, R. L. Horst and L. A. G. Armas, *J. Clin. Endocrinol. Metab.*, 2011, **96**, E447–E452.
3 P. Lips, *Prog. Biophys. Mol. Biol.*, 2006, **92**, 4–8.
4 D. Chauhan, R. Kumar, A. K. Panda and P. R. Solanki, *J. Mater. Res. Technol.*, 2019, **8**, 5490–5503.
5 A. M. Mondul, S. J. Weinstein, K. A. Moy, S. Männistö and D. Albanes, *Cancer Epidemiol., Biomarkers Prev.*, 2016, **25**, 665–669.
6 A. R. Kristal, C. Till, X. Song, C. M. Tangen, P. J. Goodman, M. L. Neuhauser, J. M. Schenk, I. M. Thompson, F. L. Meyskens, G. E. Goodman, L. M. Minasian, H. L. Parnes and E. A. Klein, *Cancer Epidemiol., Biomarkers Prev.*, 2014, **23**, 1494–1504.
7 C. S. Stokes, F. Lammert and D. A. Volmer, *Anticancer Res.*, 2018, **38**(2), 1137–1144, DOI: **10.21873/anticanres.12332**.
8 J. Chen, F. Ran, Q. Chen, D. Luo, W. Ma, T. Han, C. Wang and C. Wang, *RSC Adv.*, 2019, **9**, 4463–4468.
9 G. Brandhorst, F. Streit, J. Kratzsch, J. Schiettecatte, H. J. Roth, P. B. Luppa, A. Körner, W. Kiess, L. Binder, M. Oellerich and N. von Ahsen, *Clin. Biochem.*, 2011, **44**, 264–267.
10 H. Chen and X. Zhang, *Electrophoresis*, 2008, **29**, 3406–3413.
11 S. Shaktawat, R. Verma, K. R. Singh and J. Singh, *Sustainable Food Technol.*, 2024, **2**, 447–460.
12 S. Sakhtawat, S. K. Yadav, K. R. B. Singh, D. Kumar and J. Singh, *J. Mol. Liq.*, 2024, **402**, 124711.
13 C. Hu, D.-P. Yang, Z. Wang, L. Yu, J. Zhang and N. Jia, *Anal. Chem.*, 2013, **85**, 5200–5206.
14 M. Gachpazan, B. Hatamluyi, Z. Meshkat, M. Rezayi, S. B. Tavakoly Sany, A. Gholoobi, M. Ghayour-Mobarhan and H. R. Rahimi, *Microchem. J.*, 2023, **193**, 109186.
15 K. Bindu, T. Anusha and P. K. Brahman, *Chem. Phys. Lett.*, 2025, **865**, 141936.
16 S. C. Barman, Y. Jin, J. K. El-Demellawi, S. Thomas, N. Wehbe, Y. Lei, M. K. Hota, X. Xu, E. A. Hasan, O. F. Mohammed, O. M. Bakr, D. Alsulaiman and H. N. Alshareef, *Commun. Mater.*, 2025, **6**, 31.
17 A. Kaur, S. Rana, A. Bharti, G. R. Chaudhary and N. Prabhakar, *Microchim. Acta*, 2021, **188**, 222.
18 T. Liu, L. Finn, M. Yu, H. Wang, T. Zhai, X. Lu, Y. Tong and Y. Li, *Nano Lett.*, 2014, **14**, 2522–2527.
19 Y. Song, T. Liu, X. Xu, D. Feng, Y. Li and X. Liu, *Adv. Funct. Mater.*, 2015, **25**, 4626–4632.
20 N. Singh, *Polym. Bull.*, 2022, **79**, 6929–7007.
21 A. Nagaraj, D. Govindaraj and M. Rajan, *Emergent Mater.*, 2018, **1**, 25–33.
22 M. Farbod, E. Elahiasl and S. S. Shojaeenezhad, *J. Appl. Electrochem.*, 2023, **53**, 1623–1630.
23 Y. Wang, R. Song, L. Li, R. Fu, Z. Liu and B. Li, *Appl. Sci.*, 2021, **12**, 58.
24 A. Agarwal, H. L. Senevirathna, S. H. Koo, C. S. L. Wong, T. S. K. Lim, F. C. Ng, F. Anariba and P. Wu, *Sci. Rep.*, 2023, **13**, 13290.
25 S. A. Kumar, J. S. Shankar, B. K. Periyasamy and S. K. Nayak, *Phys. Chem. Chem. Phys.*, 2021, **23**, 22804–22816.
26 C. Xu, A. R. Puente-Santiago, D. Rodríguez-Padrón, A. Caballero, A. M. Balu, A. A. Romero, M. J. Muñoz-Batista and R. Luque, *ACS Appl. Energy Mater.*, 2019, **2**, 2161–2168.
27 A. J. Bonon, M. Weck, E. A. Bonfante and P. G. Coelho, *Mater. Sci. Eng., C*, 2016, **69**, 905–913.
28 K. I. Hadjiivanov, D. A. Panayotov, M. Y. Mihaylov, E. Z. Ivanova, K. K. Chakarova, S. M. Andonova and N. L. Drenchev, *Chem. Rev.*, 2021, **121**, 1286–1424.
29 B.-H. Lv, W. Tan, C.-C. Zhu, X. Shang and L. Zhang, *Med. Sci. Monit.*, 2018, **24**, 7532–7540.
30 L. Yang, P. W. May, L. Yin, J. A. Smith and K. N. Rosser, *J. Nanopart. Res.*, 2007, **9**, 1181–1185.
31 M. Šetka, R. Calavia, L. Vojkůvka, E. Llobet, J. Drbohlavová and S. Vallejos, *Sci. Rep.*, 2019, **9**, 8465.
32 R. V. Poonguzhali, M. Srimathi, E. R. Kumar, N. Arunadevi, H. O. Elansary, A. A. A. Abdelbacki and S. A. M. Abdelmohsen, *Ceram. Int.*, 2022, **48**, 27774–27778.
33 F. Zaaeri, M. Khoobi, M. Rouini and H. Akbari Javar, *Int. J. Polym. Mater. Polym. Biomater.*, 2018, **67**, 967–977.
34 J. Zhang, H. Liu, Y. Gu, J. Zhang, X. Zhang and X. Qi, *J. Mater. Sci.: Mater. Electron.*, 2022, **33**, 9918–9929.
35 L. Zhao, J. Zhao, T. Wu, M. Zhao, W. Yan, Y. Zhang, H. Li, Y. Wang, T. Xiao and Y. Zhao, *Nanomaterials*, 2019, **9**, 406.
36 K. N. Patil, D. Prasad, J. T. Bhanushali, B. Kakade, A. H. Jadhav and B. M. Nagaraja, *New J. Chem.*, 2021, **45**, 5659–5681.
37 M. R. Salvadori, R. A. Ando, C. A. O. Nascimento and B. Corrêa, *J. Environ. Sci. Health, Part A: Toxic/Hazard. Subst. Environ. Eng.*, 2017, **52**, 1112–1120.
38 M. Feng, W. Lu, Y. Zhou, R. Zhen, H. He, Y. Wang and C. Li, *Sci. Rep.*, 2020, **10**, 15370.
39 J. Cao, Y. Wang, J. Chen, X. Li, F. C. Walsh, J.-H. Ouyang, D. Jia and Y. Zhou, *J. Mater. Chem. A*, 2015, **3**, 14445–14457.
40 K. Tian, J. Wang, L. Cao, W. Yang, W. Guo, S. Liu, W. Li, F. Wang, X. Li, Z. Xu, Z. Wang, H. Wang and Y. Hou, *Nat. Commun.*, 2020, **11**, 3884.
41 T. Sharifi, G. Hu, X. Jia and T. Wågberg, *ACS Nano*, 2012, **6**, 8904–8912.
42 Z. Wang, H. Guo, R. Gui, H. Jin, J. Xia and F. Zhang, *Sens. Actuators, B*, 2018, **255**, 2069–2077.
43 N. Elgrishi, K. J. Rountree, B. D. McCarthy, E. S. Rountree, T. T. Eisenhart and J. L. Dempsey, *J. Chem. Educ.*, 2018, **95**, 197–206.
44 X. Ma, L. Deng, Z. Zou, Z. Pan, L. Feng, Z. Huang, Z. Liang, X. Liu, M. Li, Z. Su and H. Zheng, *Talanta*, 2024, **271**, 125646.
45 G. Ruhi and S. K. Dhawan, *Modern Electrochemical Methods in Nano, Surface and Corrosion Science*, InTech, 2014.
46 S. Mansoor, S. Shahid, K. Ashiq, N. Alwadai, M. Javed, S. Iqbal, U. Fatima, S. Zaman, M. Nazim Sarwar, F. H. Alshammari, E. B. Elkaeed, N. S. Awwad and H. A. Ibrahium, *Inorg. Chem. Commun.*, 2022, **142**, 109702.
47 H.-L. Shuai, K.-J. Huang, W.-J. Zhang, X. Cao and M.-P. Jia, *Sens. Actuators, B*, 2017, **243**, 403–411.
48 H. A. Yones, L. Zhu, B. Shao, S. Zhang, H. Xie, X. Li and W. Sun, *Int. J. Electrochem. Sci.*, 2021, **16**, 210225.
49 E. P. Randviir and C. E. Banks, *Anal. Methods*, 2022, **14**, 4602–4624.
50 F. Polli, C. D'Agostino, R. Zumpano, V. De Martino, G. Favero, L. Colangelo, S. Minisola and F. Mazzei, *Talanta*, 2023, **251**, 123755.

51 H. S. Magar, P. K. Brahman and R. Y. A. Hassan, *Biosens. Bioelectron. X*, 2022, **10**, 100124.
52 S. Yin, Y. Li, M. N. Hossain, C. Sun and H.-B. Kraatz, *Sens. Actuators, B*, 2021, **340**, 129945.
53 K. Men, Y. Chen, J. Liu and D. Wei, *Int. J. Electrochem. Sci.*, 2017, **12**, 9555–9564.
54 D. Chauhan, P. K. Gupta and P. R. Solanki, *Mater. Sci. Eng., C*, 2018, **93**, 145–156.